# Measurement of the b-jet cross section at Vs=1.96 TeV

Peters, O.

**Publication date**
2003

# Chapter 5

# Muon + Jet cross section

This analysis uses data taken with the DØ detector in the period February $28^{th}$ until May $10^{th}$, 2002. The sample is divided in 4 parts, with each part corresponding to a specific trigger setting. Events in these samples are then selected based on trigger, physics and quality criteria, namely:

- The run is qualified as good in the run quality database. This requires, among others, a fully operational central muon system and calorimeter, an operating toroid magnet and no significant other hardware or trigger problems during the run;
- A muon + jet Level 1 trigger requirement, $mu1ptxatxx\_CJT5$, as described in section 3.4;
- The presence of a reconstructed muon and a reconstructed jet, with the additional constraint that the muon lies in a cone of radius $\delta R(jet, \mu) < 0.7$ around the jet axis, where $\delta R = \sqrt{(\Delta\eta)^2 + (\Delta\phi)^2}$.

Table 5.1 lists the resulting data sample, containing 361,037 events, corresponding to a total integrated luminosity of 3.4 $\text{pb}^{-1}$.

In this chapter, we will first discuss the identification criteria for muons and jets before proceeding with the calculation of the $\mu$+jet cross section.

## 5.1 Muon Identification

Due to the low reconstruction efficiency of tracks in the central tracking system during most of the data taking period, the standard muon reconstruction and identification cannot use the central tracking, but has to rely solely on the information of the muon system. To ensure a reasonable momentum and direction measurement of the muon,

| Trigger | Number of events | Integrated luminosity ($nb^{-1}$) |
|---|---|---|
| global_CalMuon4.20 | 92900 | 862.7 |
| global_CalMuon5.00 | 33201 | 331.1 |
| global_CalMuon5.01 | 209190 | 2003.0 |
| global_CalMuon5.10 | 25746 | 246.0 |
| Total | 361037 | 3442.8 |

Table 5.1: *Data sample used in the analysis.*

it is required that the muon passes all three layers and hits a minimum number of detector components in these layers:

- At least 2 wire hits in the A-layer;
- At least 1 matching scintillator hit in the A-layer;
- At least 3 wire hits in the combined B- and C-layer;
- At least 1 matching scintillator hit in the B- or C-layer.

In addition, the fit of the A and B/C layer segments is required to converge. This fit does not always converge, which causes the inefficiency shown in table 4.4 and discussed in section 4.2.4 (page 73). Furthermore, kinematic cuts are applied to the muon:

- $p_T^{\mu} > 6$ GeV/c, to be well above the implicit cut of around 3 GeV/c that a muon requires to penetrate the iron core of the muon toroid;
- $|\eta_{\mu}| < 0.8$, to avoid the overlap regions between the forward and central system at $|\eta| \approx 1$. This $\eta$ is measured by the muon system.

Figure 5.1 shows the $p_T, \eta$ and $\phi$ distributions of the muon after applying the above selection criteria. Even though the $\eta$ distribution is symmetric around $\eta = 0$, as expected, it falls rapidly. This can be explained by the combined effect of the Level 1 trigger efficiency (see figure 3.5) and the reconstruction efficiency (see figure 4.16).

The $\phi$ distribution clearly shows the hole in the detector at $\frac{5\pi}{4} < \phi < \frac{7\pi}{4}$, as well as the octant boundaries at $\phi = \frac{\pi}{4}$ and $\phi = \frac{3\pi}{4}$, where the muon wire chambers change orientation (the effect of the octant boundaries at $\phi = \frac{5\pi}{4}$ and $\phi = \frac{7\pi}{4}$ are also present but obscured by the larger effect of the hole in the bottom). The $p_T$ of the muon is corrected for the energy loss of the muon in the calorimeter, due to ionization. This loss is approximated by a parameterization which is a function of the $p_T$ and $\eta$ of the muon, based on Run I measurements. The correction is around 2 GeV, as is shown by figure 5.2.

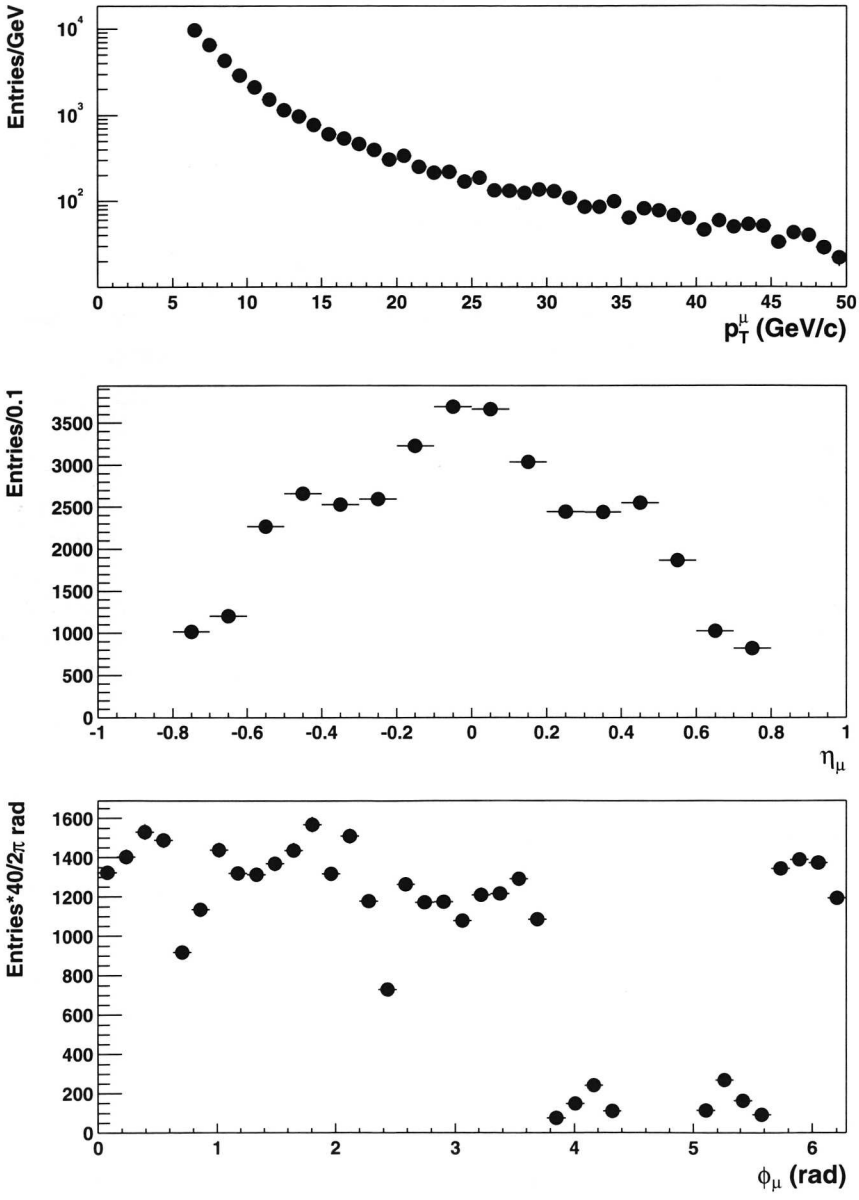


Figure 5.1: *$p_T, \eta$ and $\phi$ distributions of reconstructed muons, after applying kinematic cuts. The statistical errors on the data points are so small that they are hidden by the data points.*

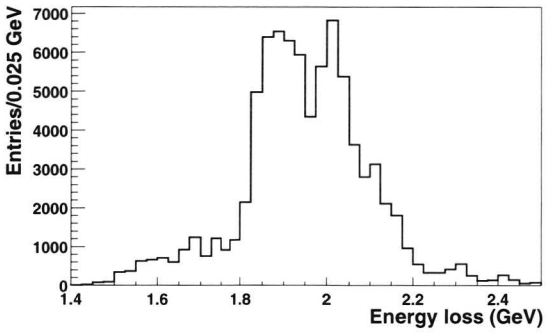


Figure 5.2: *Energy loss of a muon as it traverses the calorimeter.*

### 5.1.1 Cosmic ray contamination

A major source of background to muons produced in the collisions are cosmic ray muons that pass through the muon detector and mimic a muon coming from a collision. As has been shown in Run I [56], the requirement of the jet association removes the majority of this contamination. This effect can also be seen if we select tight muons associated with jets, in events that are taken on a jet trigger, and count how many of these muons have a scintillator time that is outside the trigger gate, i.e. cosmic ray muons. This number turns out to be of the order of $(0.2 \pm 0.05\%)$, and can therefore safely be neglected.

### 5.1.2 Punch through

A possible irreducible background to genuine muons are pions that punch through the calorimeter and the muon toroid, faking a muon. In Run I this effect was investigated, and no punch through was observed for jets with $E_T^{jet} < 200$ GeV [57]. To investigate this effect in the (for this particular effect unchanged) Run II detector, we select a data sample of reconstructed muons and jets, with the muon in a cone of $\delta R < 0.7$ of the jet axis. If the muon is caused by punch-through, we expect the number of hits in the A-layer of the muon system around the muon to increase with increasing $E_T^{jet}$. As can be seen in figure 5.3, no dependance of the number of A-layer hits is observed (a similar plot can be made for the number of B- and C-layer hits), and the amount of punch through can be ignored.

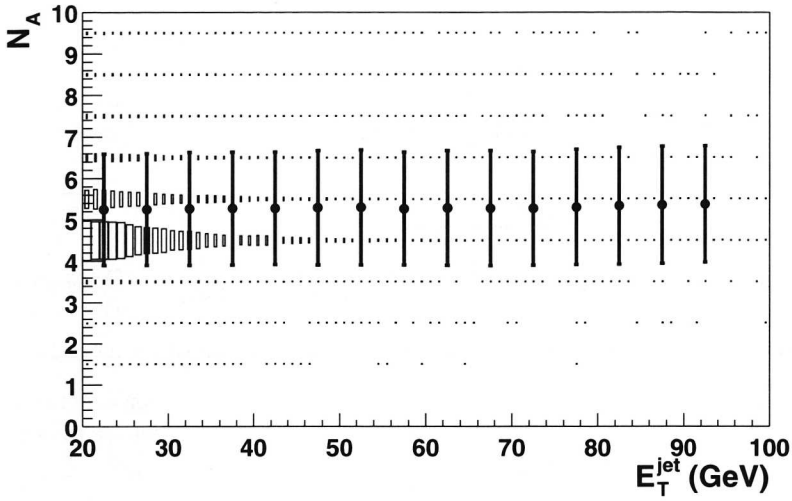


Figure 5.3: *Number of hits around a muon in the A-layer of the muon system, as a function of $E_T^{jet}$. The size of the boxes represents the number of entries in each bin. The points represent the averages in each $E_T^{jet}$ bin, with the errors representing the spread, which is defined as the RMS of the distribution in each vertical slice.*

## 5.2 Jet Selection and Identification

The majority of the background to physics jets consists of hot cells, which fake an energy deposit due to electronic noise. Even though these are partially removed at the readout level and by a hot cell suppression algorithm, some still remain and are reconstructed as fake jets. To suppress these jets, the following cuts are applied (see figure 5.4):

- Hot Fraction $< 10$: the ratio in energy between the most energetic cell and the next to most energetic cell has to be lower than 10. A higher ratio points to an unbalanced jet in which the highest energy cell is probably a hot cell;

- $1 <$ n90 $< 30$: n90 is the number of calorimeter towers which contain 90% of the jet energy. If this number is 1, this again points to an unbalanced jet consisting of one tower. If it is greater than 30, the jet consists of a high number of towers which each contain little energy. These are mainly jets consisting completely of noisy cells;

- Coarse Hadronic Fraction (CHF) $< 0.4$: The fraction of the total energy of the jet in the outer (hadronic) layer of the calorimeter. A coarse hadronic fraction of more than 0.4 is highly unlikely for genuine physics jets;

- Electromagnetic Fraction (EMF) between 0.05 and 0.95: electrons deposit more than 95% of their energy in the electromagnetic calorimeter. The lower bound indicates hot cells in the hadronic calorimeter.

In addition, the following criteria have to be met:

- $|\eta| < 0.6$, to avoid the effects of the jets pointing to the Inter Cryostat region, where the jets are poorly measured due to the gap between the central and forward calorimeters;

- $E_T > 20$ GeV, to be well above the cut-off energy in the jet reconstruction, where $E_T$ is the transverse energy of the jet, corrected by applying the Jet Energy Scale correction.

The resulting $E_T, \eta$ and $\phi$ distributions of the reconstructed jets are displayed in figure 5.5. The $E_T$ distribution turns on at 14.4 GeV, which is caused by the cut-off in the jet reconstruction algorithm, as well as the jet reconstruction efficiency which is only fully efficient above 20 GeV. The $\eta$ distribution is flat in the region of interest for this analysis, and drops at higher $\eta$ values due to the reduced calorimeter coverage in the intercryostat region. The $\phi$ distribution shows an eight-fold structure, due to the requirement of an associated muon with $\delta R(jet, \mu) < 0.7$. Less muons are reconstructed in the region $\frac{5\pi}{4} < \phi < \frac{7\pi}{4}$, resulting in less associated jets in that region. Also, other side jets in the region $\frac{\pi}{4} < \phi < \frac{3\pi}{4}$ are suppressed by this effect.

### 5.2.1 Jet ID Efficiency

Not only do the jet ID cuts as explained in the previous section cut out the fake jets, they also remove a number of good jets for which a correction needs to be applied. The extent of this correction is calculated using di-jet events, in which one of the jets passes the ID criteria, and furthermore:

- Both jets have $|\eta| < 0.6$ and $E_T > 20$ GeV, to be in the same fiducial volume as the jets in the data sample;

- The jets are back-to-back: $\Delta\phi > 175°$, and $\not\!\!E_T < 0.7 E_T^{leading\ jet}$, to ensure a proper di-jet event;

- $E_{tot} < 2$ TeV, to remove events with noisy calorimeter readout.

The ID efficiency can be extracted from this sample using the following definition:

$$\epsilon_{ID} = \frac{Number\ of\ other\ side\ jets\ passing\ ID\ cuts}{Total\ number\ of\ other\ side\ jets} \tag{5.1}$$

This efficiency is shown as a function of jet $E_T, \eta$ and $\phi$ in figure 5.6, and averages to $(94.2 \pm 0.1\%)$. The ID efficiency as a function of jet $E_T$ shows a turn-on curve for jets below 40 GeV. This turn-on curve is caused by the cut on the electromagnetic fraction of the jet - low energy jets deposit a higher fraction of their energy in the first (electromagnetic) layers of the calorimeter. This is demonstrated in figure 5.6 by the small crosses, which represent the jet ID efficiency without the EMF cuts. Without these cuts, the ID efficiency averages to $(98.7 \pm 0.1\%)$.

An additional event topology that affects this efficiency measurement is back to back $\gamma$+jet events, in which the jet passes the ID cuts listed above, and enters the denominator of equation 5.1. The photon normally does not pass the ID cuts, which lowers the measured ID efficiency. To measure the extent of this effect, we count the number of such events in the Monte Carlo simulation compared to the number of di-jet events. This ratio results in $(0.05 \pm 0.05)\%$, indicating that these event topologies do not have a significant effect on the jet ID measurement.

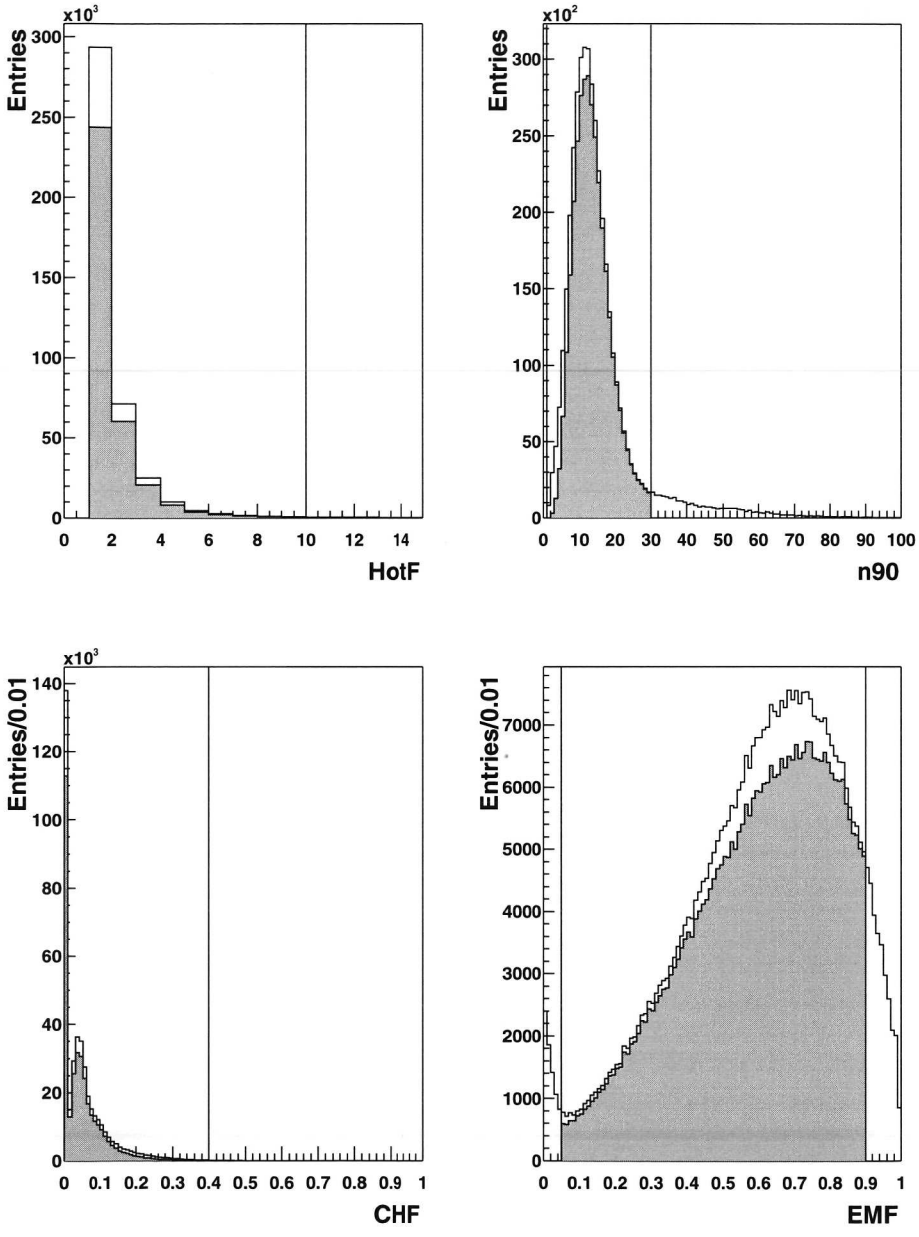


Figure 5.4: *Properties of jets used to suppress fake jets, before (open histograms) and after (solid grey histograms) ID cuts. The quantities on the horizontal axes are explained in the text.*

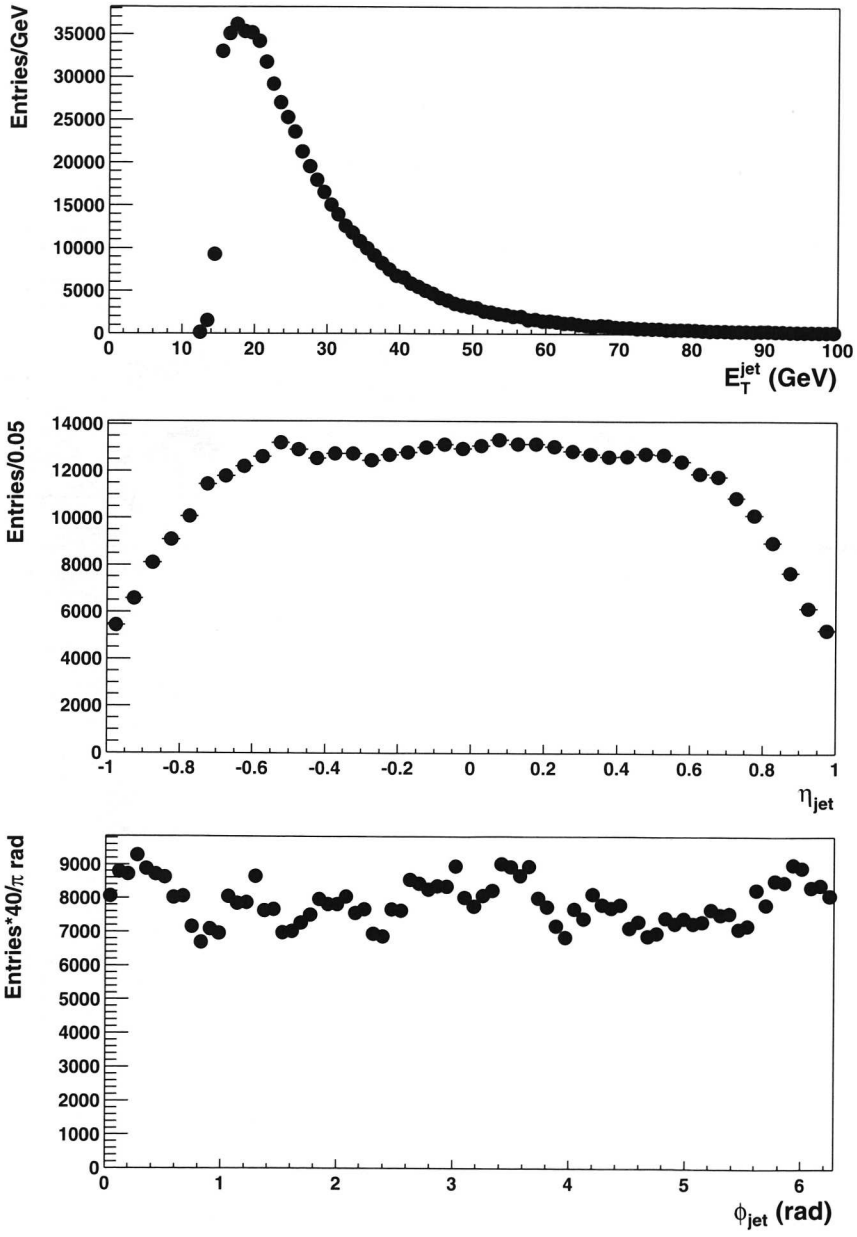


Figure 5.5: *$E_T$, $\eta$ and $\phi$ distribution of reconstructed jets, after selection and kinematic cuts.*

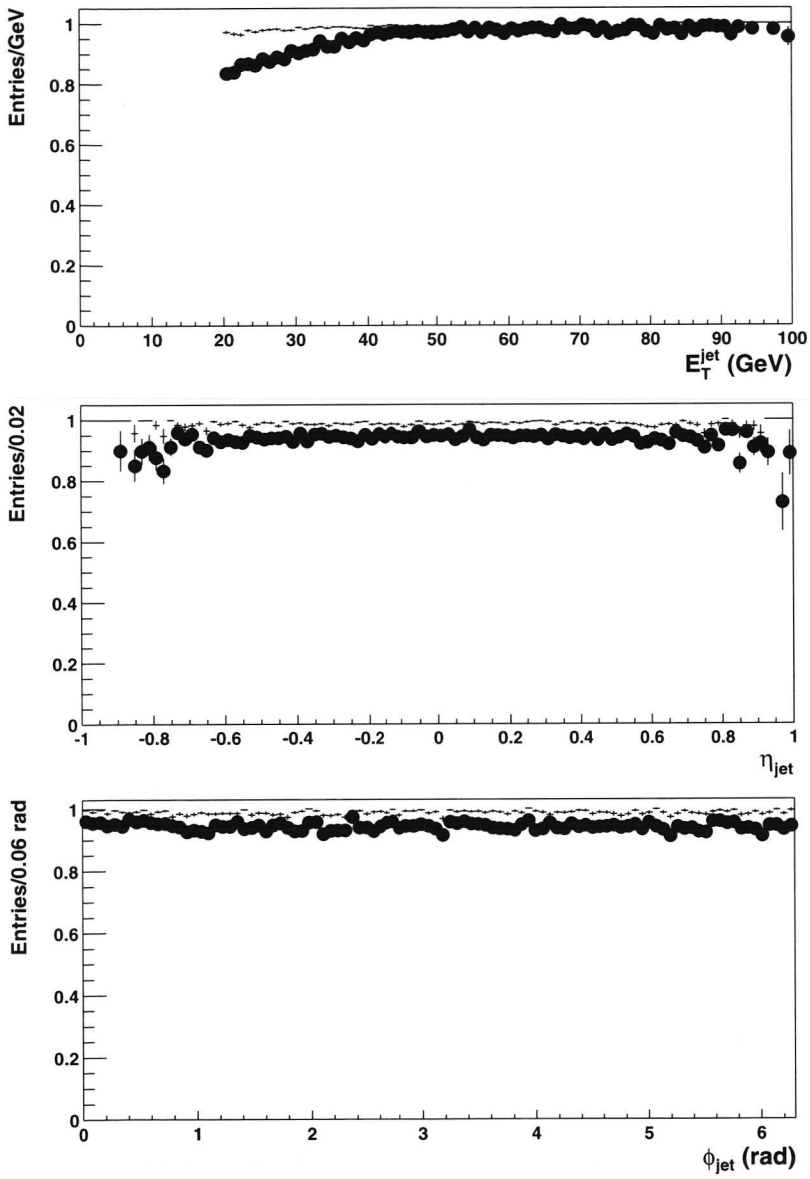


Figure 5.6: *Jet ID efficiency as function of $E_T^{jet}$, $\eta$ and $\phi$. Black dots represent the efficiency after all cuts, the crosses represent the efficiency without the EMF cuts.*

## 5.3 $\mu$+jet cross section measurement

To conclude this chapter we will measure the differential cross section of $\mu$+jet events as a function of the calorimeter transverse jet energy, $\mathrm{d}\sigma/\mathrm{d}E_T^{jet_{Cal}}$. This jet energy is corrected for the Jet Energy Scale, and for the ionization energy that the muon deposits on average in the calorimeter. This quantity is illustrated in figure 5.7. The measurement of the differential $\mu$+jet cross section is the first step towards the $b$-jet cross section measurement.

Using the data sample described earlier in this chapter, the first measurement is the number of events in each $E_T^{jet_{Cal}}$ bin, $\mathrm{d}N/\mathrm{d}E_T^{jet_{Cal}}$. Both the muon and the jet in each event have to pass the identification cuts as discussed in this chapter, as well as the following kinematic cuts:

- $E_T^{jet_{Cal}} > 20$ GeV;
- $|\eta^{jet_{Cal}}| < 0.6$;
- $p_T^{\mu} > 6$ GeV/c;
- $|\eta_{\mu}| < 0.8$;
- $\delta R(jet_{Cal}, \mu) < 0.7$.

This results in the distribution of $\mathrm{d}N/\mathrm{d}E_T^{jet_{Cal}}$ as shown in figure 5.8, where the horizontal lines represent the bin sizes used which are chosen according to the jet energy resolution.

To measure the differential cross section, each event needs to be scaled with the detection efficiency for that event, and must be normalized to the total integrated luminosity:

$$\frac{\mathrm{d}\sigma}{\mathrm{d}E_T^{jet_{Cal}}} = \frac{1}{\int \mathcal{L}dt} \frac{1}{\epsilon(\mu, jet_{Cal})} \frac{\mathrm{d}N}{\mathrm{d}E_T^{jet_{Cal}}} \tag{5.2}$$

Here, $\int \mathcal{L}dt$ is the total integrated luminosity and $\epsilon(\mu, jet_{Cal})$ is the combined efficiency of all trigger, reconstruction and identification efficiencies for the muons and jets in that $E_T^{jet_{Cal}}$ bin. This efficiency correction is the subject of the next section.

### 5.3.1 Efficiency corrections

The correction to the measured cross section for efficiencies is applied on a jet by jet basis. For every jet with an associated muon, the dependance of the efficiency on the $\eta, \phi$ or $p_T$ of the muon and jet is taken into account. We use the 1-dimensional distributions under the assumptions that the efficiency factorizes. The effect of the uncertainty on each efficiency is propagated to the full cross section by varying each efficiency within the errors. Each source of uncertainty is briefly explained below.

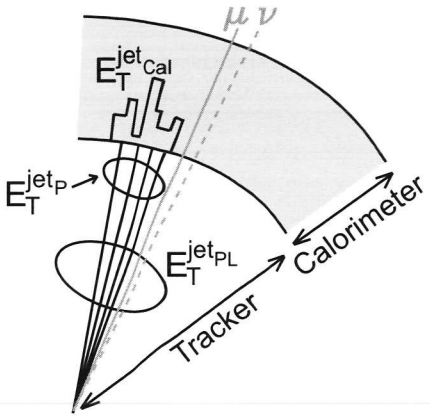


Figure 5.7: *Illustration of different jet energy scales used in the analysis. The energy that is deposited in the calorimeter by the jet, represented by the black irregular shape is denoted by* $E_T^{jet_{Cal}}$. *This energy can be unfolded to the particle level jet energy* $E_T^{jet_P}$, *which is the energy of all particles in the jet, without the muon and neutrino (shown by the solid and dashed grey lines, respectively). Adding the energy of these two particles to the jet energy results in the lepton corrected jet energy,* $E_T^{jet_{PL}}$.

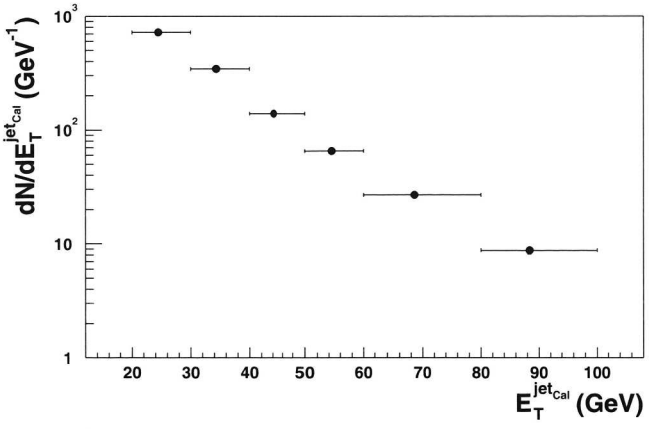


Figure 5.8: *Number of events in each* $E_T^{jet_{Cal}}$ *bin, per GeV. The statistical errors are shown, but so small that they are hidden by the data points.*

### Level 1 calorimeter trigger

The $\mu$+jet cross section is corrected for the Level 1 calorimeter trigger efficiency according to the turn-on curve shown in figure 3.3. The effect of the statistical uncertainty of the trigger efficiency on the cross section is shown by the open circles in figure 5.9. The systematic uncertainty of the trigger efficiency is dominated by the uncertainty of the Jet Energy Scale correction. This effect is not taken into account here, but will be discussed below.

### Level 1 muon trigger efficiency

The Level 1 muon trigger efficiency shows a dependance on both $p_T^\mu$ and $\eta^\mu$ (see figure 3.5). Due to statistical limitations, it is not possible to perform a full 2-dimensional calculation of the efficiency in ($p_T$, $\eta$) bins. Therefore, we first calculate the efficiency averaged over $p_T$ but taking into account the $\eta$ dependance. Then, the efficiency is calculated using an averaged $\eta$ efficiency and taking into account the $p_T$ dependance. The difference resulting from using these two different efficiencies is taken as an additional systematic error on the Level 1 muon trigger efficiency. The effect of the resulting total error on the cross section is shown by the black squares in figure 5.9.

### Muon reconstruction efficiency

The muon reconstruction efficiency depends on $p_T, \eta$, and to a lesser extent, on $\phi$ (see figure 4.16). Since the physics is invariant under rotations in $\phi$, we correct for the hole in the bottom of the detector by an overall scale factor. The dependance on $p_T$ and $\eta$ is taken into account in a similar fashion as done for the Level 1 muon trigger efficiency. The black circles in figure 5.9 show the systematic error on the cross section resulting from the errors on the muon reconstruction efficiency.

### Jet Energy Scale correction

We use the uncertainty on the Jet Energy Scale correction of typically 7%, as shown in figure 4.3, to estimate the systematic effect on the $\mu$+jet cross section. The calculation of the $\mu$+jet cross section is redone for a Jet Energy Scale correction obtained by adding (subtracting) the uncertainty to the nominal values. The resulting effects are illustrated in figure 5.9 by the open triangles. The strong dependance of the $\mu$+jet cross section on the energy scale of the jets leads to effects of 40% in the lowest $E_T$ bin.

The total systematic error is represented by the black triangles in figure 5.9. The resulting $\mu$+jet cross section, measured as a function of the calorimeter transverse jet energy, $E_T^{jet_{Cal}}$, is shown by the black dots in figure 5.10, with statistical and systematic

errors. The systematic errors dominate the total error. This differential cross section is now the input to an unfolding procedure and to the measurement of the $b$-jet cross section, as will be shown in the next chapter.

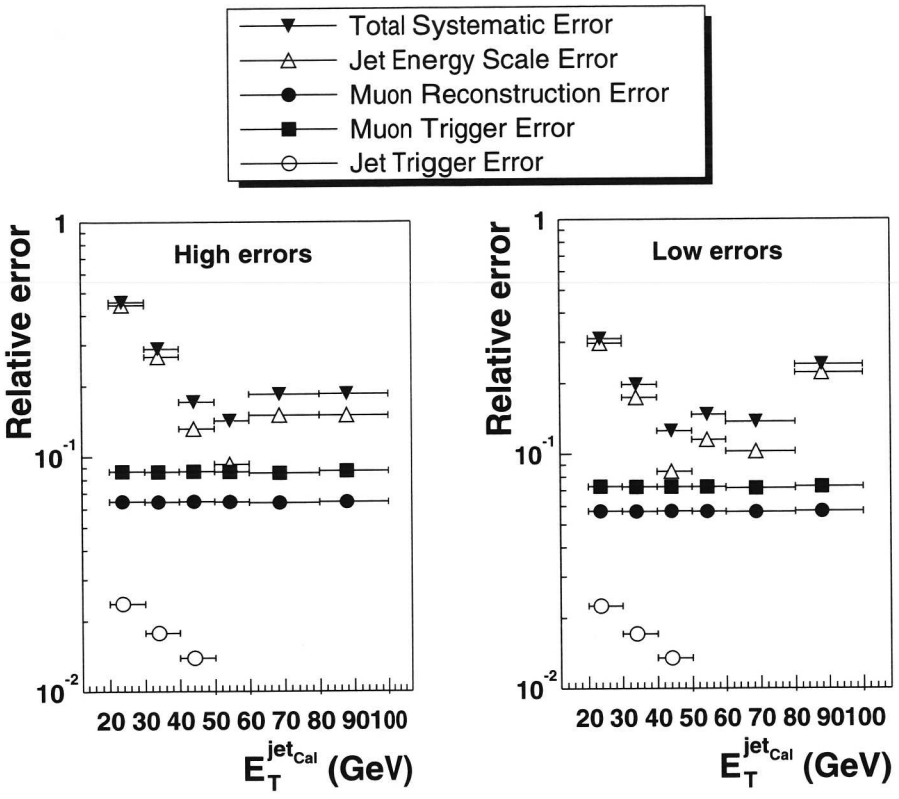


Figure 5.9: *Systematic errors on the $\mu$ + jet differential cross section, resulting from the sources listed in the text, as a function of transverse calorimeter jet energy. Since the errors are asymmetric, both the high and the low errors are shown, which result from floating the errors on each efficiency up and down, respectively.*

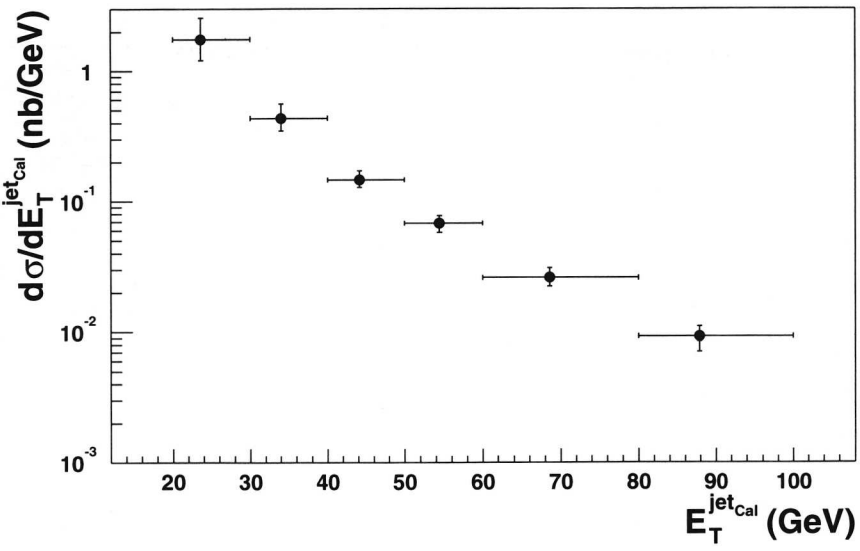


Figure 5.10: *$\mu$ + jet cross section as a function of $E_T^{jet_{Cal}}$, with full statistical and systematic errors.*